特集 卵子のエイジング　III．胚の非侵襲的評価法

9．走査型電気化学顕微鏡を用いた胚の評価法

阿部宏之（あべひろゆき）*
山形大学大学院理工学研究科バイオ化学工学専攻*

要旨

ミトコンドリアは酸素呼吸によって細胞活動に必須のエネルギー（ATP）を合成する細胞小器官であり，細胞の代謝活動や胚の発生，アポトーシスなどの重要な生物現象に関与している．したがって，高精度の細胞呼吸計測は，胚の品質やミトコンドリア呼吸機能を評価・解析するための有用な技術となる．本項では，電気化学計測技術を応用した細胞呼吸測定法を解説し，この技術の中心装置である走査型電気化学顕微鏡を用いた胚の品質評価法を紹介する．

Key Words 細胞呼吸，胚発生，電気化学計測

ミトコンドリアは酸素呼吸によって細胞活動に必須のエネルギー（ATP）を合成する細胞小器官であり，細胞の代謝活動や胚の発生，アポトーシスなどの重要な生物現象に関与している．したがって，高精度の細胞呼吸計測は，胚の品質やミトコンドリア呼吸機能を評価・解析するための有用な技術となる．本項では，電気化学計測技術を応用した細胞呼吸測定法を解説し，この技術の中心装置である走査型電気化学顕微鏡を用いた胚の品質評価法を紹介する．

電気化学計測技術を応用した細胞呼吸測定

電気化学計測法はプローブ電極による酸化還元反応を利用し，局所領域における生物反応を電気化学的に検出する技術であり，この技術の有効な装置としてマイクロ電極をプローブとする走査型電気化学顕微鏡（Scanning electrochemical microscopy：SECM）が注目されている．SECMの空間分解能は探針であるマイクロ電極径に依存するため原子や分子レベルの解析は困難であるが，局所空間での化学反応の評価やイメージング，生体材料を用いたリアルタイム解析や化学反応誘起が可能であることから，局所領域の電気化学センシングなど種々の系で用いられている[1]．たとえば，酸素の還元電位を検出できるマイクロ電極を用いることで細胞の酸素消費量（呼吸）を高感度・非侵襲的にリアルタイムで測定することができる[2]．筆者らは，SECMをベースに胚の呼吸量測定に特化したシステムとして「受精卵呼吸測定装置」の開発に成功している[3]．この測定システムは，倒立型顕微鏡，マイクロ電極の電位を一定に保持するポテンショスタット，マイクロ電極

0386-9792/11/¥100/頁/JCOPY

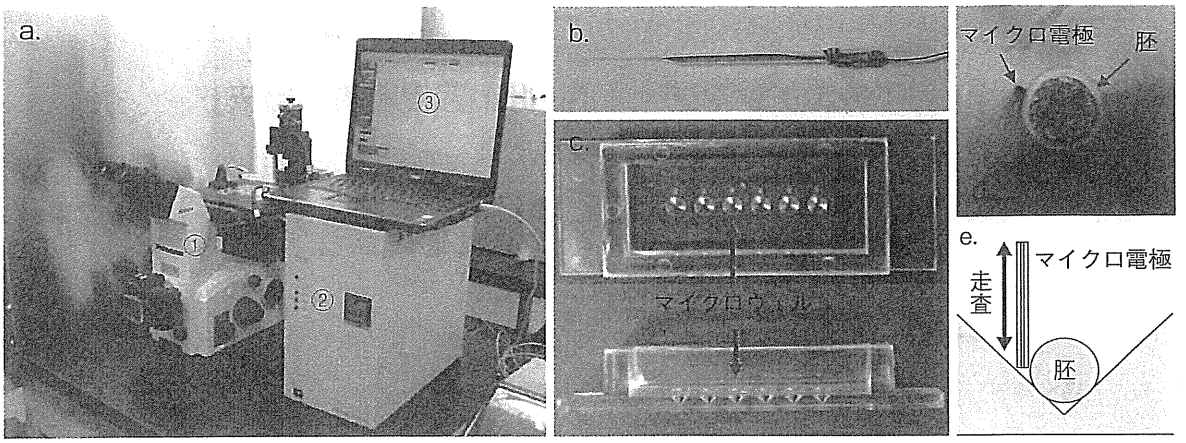

図1 電気化学計測技術を応用した超高感度細胞呼吸測定システム

(a) 走査型電気化学顕微鏡をベースに開発した「受精卵呼吸測定装置」. ①：倒立型顕微鏡，②：ポテンショスタット，③：ノートパソコン（呼吸能解析ソフトを内蔵）. (b) ディスク型白金マイクロ電極. (c) 多検体測定プレート：底面には円錐形のマイクロウェルが6穴施されている. (d) マイクロウェル底部に静置したウシ胚. (e) マイクロ電極は胚近傍を鉛直方向に挿引し，胚の酸素消費量を測定する.

の移動を制御し短時間で酸素消費量を算出する専用の解析ソフトを内蔵したノート型コンピューターにより構成されている（図1a）. 倒立型顕微鏡のステージ上には，保温プレート，マイクロ電極の3次元走査を可能とするXYZステージが設置されており，気相条件を制御できる測定用チャンバーの設置も可能である.

「受精卵呼吸測定装置」による胚の呼吸量測定

「受精卵呼吸測定装置」を用いた呼吸量測定には，超高感度のディスク型マイクロ電極（図1b），専用の多検体測定プレートと受精卵培養液をベースに調製した非侵襲測定液を用いる. 多検体測定プレートは測定操作の簡易化を目的に開発され，プレートの底面には円錐形のマイクロウェル6穴が施されている（図1c）. マイクロ電極を用いた電気化学計測は高精度計測技術であることから，呼吸測定には微弱な酸素還元電流計測に影響を与えず，かつ細胞の呼吸機能に影響を及ぼさない成分組成の測定液を用いる. たとえば，電気化学計測には比較的単純な成分で調製されているHTF（Human tubal fluid）培地が有効である. 測定液を満たしたマイクロウェル内に胚を導入した後，ウェルの底部中心に静置する（図1d）. マイクロ電極を胚の透明帯直近に手動で移動したのち，酸素が還元可能な−0.6 V *vs.* Ag/AgClに電位を保持した状態でコンピューター制御により透明帯近傍を鉛直（Z軸）方向に挿引する（図1e）. 通常，1試料あたりマイクロ電極を2〜3回走査し，呼吸によって胚近傍に生じる酸素濃度勾配を測定する. マイクロ電極走査後，胚の酸素消費量は球面拡散理論式を基盤とする呼吸解析ソフトを用いて，呼吸によって胚近傍に生じる酸素濃度差から算出する[4].

胚のミトコンドリア呼吸機能解析

「受精卵呼吸測定装置」を用いて，種々の哺乳動物胚の呼吸量測定に成功している. ほとんどの動物胚では，発生過程において8細胞期までの発生初期では酸素消費量は少なく，桑実胚から胚盤胞にかけて顕著に呼吸量が増加する（表1）. 呼吸測定の有用性を評価するために呼吸能とミトコンドリアの微細構造との関係を調べ

た結果，呼吸活性の低い8細胞期まではミトコンドリアのほとんどは未成熟であるが，桑実胚から胚盤胞にかけてミトコンドリアの顕著な発達（クリステの拡張）が認められ，呼吸量の増加とミトコンドリアの発達がリンクしていることがわかる（図2）．また，ミトコンドリア内膜に存在し酸素呼吸に関与するシトクロムcオキシダーゼ（COX）の遺伝子発現と呼吸量の増加が一致することが明らかにされている[5]．このように，「受精卵呼吸測定装置」は呼吸量を指標に，胚のミトコンドリア呼吸機能を高精度で解析できる有用な測定システムである．

表1　ウシ体外受精胚の発生過程における呼吸量変化

発生ステージ	測定胚数	酸素消費量（$\times 10^{14}$/mol・s^{-1}）
2細胞	15	0.46±0.05[a]
4細胞	17	0.45±0.03[a]
8細胞	18	0.46±0.02[a]
桑実胚	48	1.03±0.05[b]
胚盤胞	55	1.86±0.07[c]
孵化胚盤胞	24	3.01±0.07[d]

異符号間で有意差あり（$P<0.05$）．

呼吸機能解析と胚のクオリティー評価

体外受精・胚移植（in vitro fertilization and embryo transfer：IVF-ET）は，最も有効な不妊治療法の一つである．一般にIVF-ETでは，IVFによって得られた複数の胚のなかから移植する胚を選択する．胚移植前に最も質的に良好な胚を選択することは，妊娠率の向上，多胎妊娠の回避，流産率の低下のために有効である．現在，胚の品質評価は形態観察による方法が一般的である．形態的評価法は，簡単・迅速で無侵襲的な方法であることから，現状では最も有効な胚のクオリティー評価法であるといえる．

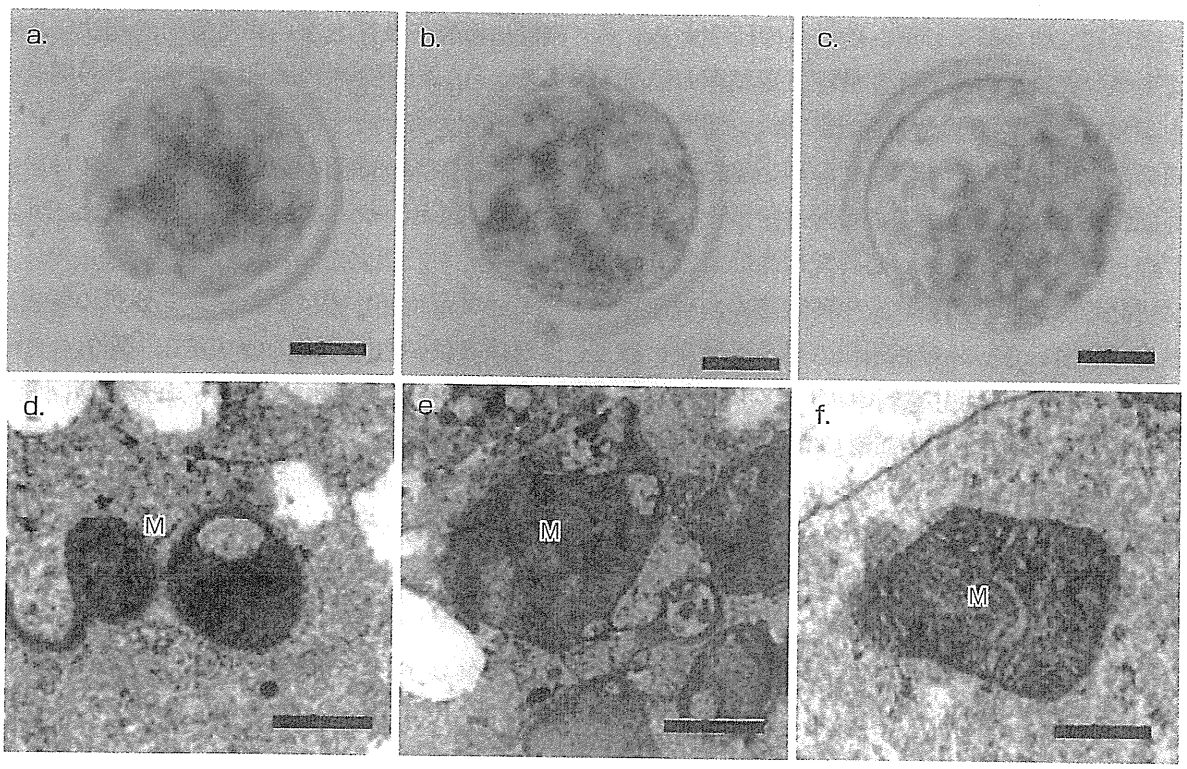

図2　ウシ胚の発生過程における胚の形態（a-c）とミトコンドリアの微細構造（d-f）
a，d：8細胞期胚，b，e：桑実胚，c，f：胚盤胞．M：ミトコンドリア．ミトコンドリアの発達と呼吸量の増加は一致する．スケールバーは，a-c：20 μm，d-f：0.5 μm を示す．

表2 ウシ胚の呼吸量と妊娠率の関係

移植時の発生ステージ	酸素消費量 ($F\times10^{14}$/mol・s^{-1})	受胎胚数/移植胚数 (妊娠率%)
胚盤胞	$F\geq1.0$	21/36 (58.3)
	$F<1.0$	0/6 (0)
初期胚盤胞	$F\geq0.8$	16/25 (64.0)
	$F<0.8$	0/6 (0)
桑実胚	$F\geq0.5$	17/28 (60.7)
	$F<0.5$	1/12 (8.3)

しかし，評価の基準となる形態的特徴は定量性に欠けるため，判定結果が観察者の主観に左右される可能性がある．筆者らは，形態良好胚ではミトコンドリアは正常に発達しているが，形態不良胚や発生停止胚ではミトコンドリアの多くは未成熟あるいは退行していることを発見している[6)7)]．ミトコンドリアは酸化的リン酸化(呼吸)により細胞活動に必須のエネルギーであるアデノシン三リン酸(ATP)を産生し，胚の発生等に深く関与している．これらの研究から，ミトコンドリア呼吸活性を指標に受精卵の品質を評価するという独創的発想に至り，「受精卵呼吸測定装置」を用いた精度の高い受精卵品質評価システムの開発を進めてきた．

これまでのウシを用いた研究において，胚の品質と呼吸活性の関係を示す興味深い研究成果が得られている．呼吸測定後の胚を借腹牛に移植し胚の呼吸活性と受胎率の関係を調べた結果，移植前の呼吸量が基準値以上（胚盤胞で 1.0×10^{14}/mol・sec^{-1}，初期胚盤胞で 0.8×10^{14}/mol・sec^{-1}，桑実胚で 0.5×10^{14}/mol・sec^{-1}）の胚を移植した場合，60%以上の高い妊娠率が得られている（表2）．一方，呼吸量が基準値以下の胚は，ほとんど受胎しない．この研究結果により，SECMをベースに開発した「受精卵呼吸測定装置」は，妊娠が期待できる品質良好胚の選別に有効なシステムであることが示された[8)]．

表3 ヒト胚（余剰胚）の胚発生過程における酸素消費量（呼吸量）変化

発生ステージ	胚数	酸素消費量 ($F\times10^{14}$/mol・s^{-1})
2−8細胞	18	0.51±0.05
桑実胚	5	0.61±0.11
初期胚盤胞	13	0.72±0.06
胚盤胞	4	1.01±0.02

ヒト胚の呼吸機能解析と探索的臨床研究

「受精卵呼吸測定装置」は，短時間で非侵襲的に細胞の呼吸量を測定できることから，不妊治療などの医療応用が期待できる．ウシやマウスを用いた動物実験において，呼吸測定した胚を移植し誕生した産子の染色体や行動等を解析した結果，染色体異常や奇形，行動異常などの事例はまったく確認されていない．このように，「受精卵呼吸測定装置」による呼吸測定は，細胞機能に影響を及ぼさない非侵襲的計測法であることから，医療応用へ向けて安全面での問題はクリアできると考えている[9)]．

現在，探索的臨床研究として「受精卵呼吸測定装置」を用いたヒト胚の呼吸量測定と品質評価システムの確立を試みている．これまでに，ヒト胚（余剰胚）ではミトコンドリアの発達に伴い呼吸量が増加すること（表3，図3），呼吸活性の高い胚は胚盤胞への発生率が高い傾向にあることが示されている[10)]．また，形態的評価が同じ胚でも呼吸活性が大きく異なることから，呼吸測定は形態観察だけでは知ることができない胚の代謝活性を客観的に評価できる可能性を示している[11)]．これらの研究成果を踏まえ所定の倫理承認を得た後，不妊治療での臨床応用を目的に呼吸測定胚の移植試験を開始している[12)]．試験的な臨床例では，形態的評価が同じ胚が複数得られた症例において呼吸活性を指標とする評価法を導入している．これまでに形態

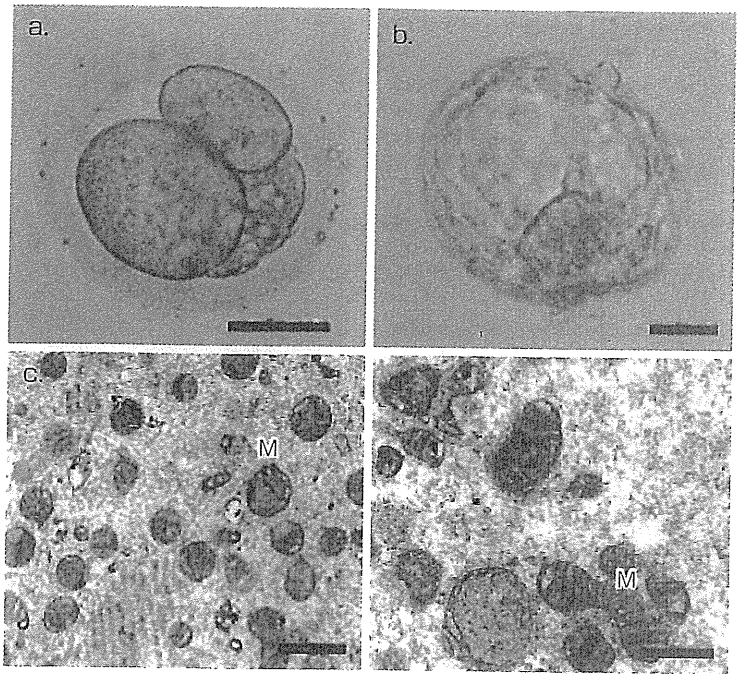

図3 ヒト胚(余剰胚)の形態(a,b)とミトコンドリアの微細形態(c,d)
a，c：2細胞期胚，b，d：拡張胚盤胞．M：ミトコンドリア．ミトコンドリアの発達と呼吸量の増加は一致する．スケールバーは，a，b＝50 μm，c，d＝0.5 μm を示す．

表4 不妊治療における探索的臨床研究

評価方法	周期数	妊娠例（%）	流産例（%）
形態＋呼吸	25	13（52.0）	1（7.6）
形態	27	8（29.6）	2（25.0）

的評価が良好で呼吸活性が最も高い胚を移植した場合，従来の形態的評価のみで評価した胚を移植した場合と比べて有意に妊娠率が向上することが示されている（表4）．このように，「受精卵呼吸測定装置」はヒト胚の品質評価においても有用なシステムであると考えられる．今後は，呼吸測定によるヒト胚品質評価の臨床的有効性を示すための多施設臨床研究を計画している．

おわりに

今後，不妊治療を望む患者の高年齢化や多様化が進み，IVF-ETによる不妊治療成績の向上には移植に供する胚の品質評価がこれまで以上に重要になってくる．精度の高い胚の品質評価を実現するためには，形態的評価法と併用できる客観性の高い品質評価法の開発が極めて重要である．本項で解説した「受精卵呼吸測定装置」は，高精度・非侵襲的に胚の呼吸代謝機能を解析できることから，新しい胚の品質評価の有効な技術としての実用化が期待される．

文 献

1) Bard AJ, Mirkin MV：Scanning Electrochemical Microscopy, Marcel Dekker, New York, 2001.
2) Shiku H, Shiraishi T, Ohya H, et al：Oxygen consumption of single bovine embryos probed with scanning electrochemical microscopy. Anal Chem 2001；73：3751-3758.
3) Abe H, Shiku H, Aoyagi S, et al：In vitro culture and evaluation of embryos for production of high quality bovine embryos, J Mamm Ova Res 2004；21：22-30.
4) Shiku H, Shiraishi T, Aoyagi S, et al：Respiration activity of single bovine embryos entrapped in cone-shaped microwell monitored by scanning electrochemical microscopy. Anal Chim Acta 2004；522：51-58.

5) 岡崎直人・他：マウス胚発生過程におけるミトコンドリア機能解析．J Mamm Ova Res 2007；24：S47.
6) Abe H, Yamashita S, et al：Accumulation of cytoplasmic lipid droplets in bovine embryos and cryotolerance of embryos developed in different culture systems using serum-free or serum-containing media. Mol Reprod Dev 2002；61：57-66.
7) Abe H, Matsuzaki S, Hoshi H：Ultrastructural differences in bovine morulae classiifed as high and low qualities by morphological evaluation. Theriogenology 2002；57：1273-1283.
8) Abe H：A non-invasive and sensitive method for measuring cellular respiration with a scanning electrochemical microscopy to evaluate embryo quality. J Mamm Ova Res 2007；24：70-78.
9) 横尾正樹・他：呼吸活性を指標とした胚の品質評価 ―マウス胚移植試験の成績と産子の正常性について―．産婦の実際 2010；59：1375-1379.
10) Utsunomiya T, Goto K, Nasu M, et al：Evaluating the quality of human embryos with a measurement of oxygen consumption by scanning electrochemical microscopy. J Mamm Ova Res 2008；25：2-7.
11) 後藤香里・他：電気化学的吸計測技術におけるヒト胚クオリティー評価と安全性，受精着床学会雑誌 2010；27：53-58.
12) 後藤香里・他：選択的単一胚移植（eSET）における移植胚選別困難例に対する呼吸量測定の有用性．産婦の実際；59：1277-1281.

著者連絡先
〒992-8510
山形県米沢市城南 4-3-16
山形大学大学院理工学研究科バイオ化学工学専攻
阿部宏之

一口メモ

私たちが開発した「受精卵呼吸測定装置」は，真核細胞に共通する細胞呼吸を計測対象としていることから，その応用範囲は極めて広いと考えています．ここで紹介した胚の品質評価のほかに，糖尿病治療における膵島の機能診断，魚介類などの鮮度評価などにも応用されています．また，この装置は，現在最も高感度・無侵襲的に細胞呼吸を測定できることから，シングルセルレベルでのリアルタイム呼吸代謝解析や，形態観察では評価が困難である卵子の品質評価にも有効であることがわかってきています．この装置がポストゲノム時代の有力な細胞機能解析システムとして，基礎研究や医療・産業分野において応用されることを期待しています．

（阿部宏之）

Influence of Tip Size on Single Yeast Cell Imaging Using Scanning Electrochemical Microscopy

*Kuniaki Nagamine, Yasufumi Takahashi, Kosuke Ino, Hitoshi Shiku, Tomokazu Matsue**

Graduate School of Environmental Studies, Tohoku University, 6-6-11, Aramaki-Aoba, Aoba, Sendai 980-8579, Japan
tel/fax: +81-22-795-7209
*e-mail: matsue@bioinfo.che.tohoku.ac.jp

Received: September 24, 2010
Accepted: January 10, 2011

Abstract
The influence of the tip reaction on the substrate generation/tip collection mode SECM imaging of a single yeast cell was investigated by using various sizes of probe electrodes in μm–nm scales because the tip reaction would disturb the concentration profile of intracellular enzyme reactant formed around the cell. GC mode measurements of a single yeast cell were performed using a dual mediator system with lipophilic menadione and hydrophilic ferricyanide. We found downscaling of the tip size enabled quantitative SECM imaging of a single cell in GC mode without disturbing the concentration profile of the mediator formed around the cell by the tip reaction.

Keywords: Scanning electrochemical microscopy, Nanoelectrodes, Single cell analysis

DOI: 10.1002/elan.201000595

1 Introduction

Quantitative analysis of intracellular enzyme activity in microbial cells including yeast cells has been required for investigation of cell physiology and cell-based diagnosis of pathologic conditions. In particular, measurement of cellular activity of a specific cell spatially localized in a densely packed cell population is helpful for revealing metabolic alteration in individual cells via cell-cell communication. This metabolic regulation is a requisite for microbial cells to survive in variable and cruel microenvironments and for some bacteria to induce pathogenic gene expression [1–4]. Therefore, development of single microbial cell analysis in a densely packed population has been expected to reveal the cell-cell communication in microbial cells and to improve the screening drugs used to inhibit pathogenic gene expression in an infectious cell.

Bioelectrochemical methods have provided the noninvasive quantitative analysis of intracellular redox enzyme activity using mediators that shuttle electrons between intracellular enzymes and the electrode placed extracellularly [5–10]. In addition, by means of scanning electrochemical microscopy (SECM), intracellular enzyme activity has been quantified in spatially localized single prokaryotic and eukaryotic cells [11–27]. In substrate generation/tip collection (GC) mode SECM, a concentration profile of intracellular enzyme reactant was detected by scanning a probe electrode above a target cell. Sensitivity of GC mode SECM is relatively high as the background signal is very low. However, when a probe electrode with a large active tip was used for GC mode imaging, the concentration profile of intracellular enzyme reactant formed around the cells might be disturbed by the consumption (or generation) of redox species at the tip itself. Downscaling of the tip size would suppress the disturbance of concentration profile and enables clear imaging of a single cell.

In this study, we investigated the influence of tip reaction on the GC mode SECM imaging of a single yeast cell by using various Pt electrode probes with tip sizes in μm–nm scales. The target intracellular enzyme was cytosolic and mitochondrial NAD(P)H-oxidizing enzymes (NOEs), which is the general term for all enzymes catalyzing electron transfer from NAD(P)H to quinone substrates. Figure 1 shows the principle of electrochemical detection of NOEs activity in the GC mode [5–10]. NOEs activity in a yeast cell was detected using a dual mediator system with lipophilic menadione and hydrophilic ferricyanide. Mauzeroll and Bard investigated the permeation of menadione through yeast cells, the intracellular formation of menadione-*S*-glutathione conjugate, and the efflux of the conjugate from the cells using GC mode SECM [28]. In this study, menadione shuttles electrons from intracellular NOEs to extracellular ferricyanide with low permeability to cell membrane, followed by ferrocyanide generation around the cell. SECM was used to monitor the ferrocyanide generation that reflects NOEs activity in yeast cell. We found that downscaling of the tip size enabled quantitative SECM imaging of a single yeast cell in GC mode without disturbing the concentration profile of mediator formed around the cell by the tip reaction.

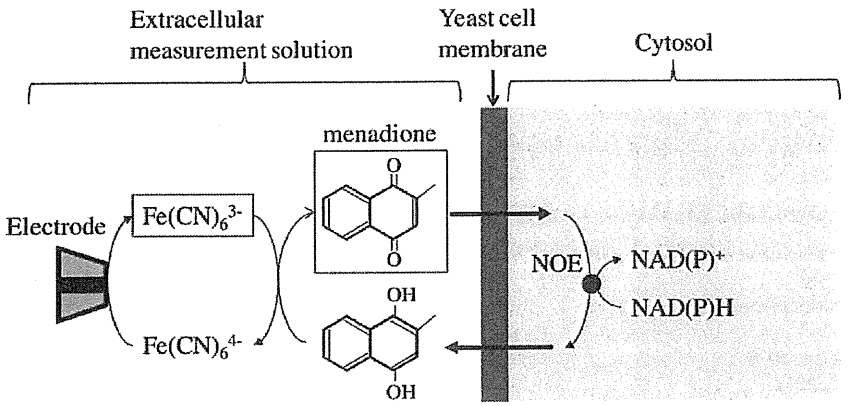

Fig. 1. Principle of electrochemical detection of NOEs activity in yeast cell. $Fe(CN)_6^{3-}$ and menadione (indicated by squares) were added to the measurement solution.

2 Experimental

2.1 Reagents

Potassium hexacyanoferrate(III), menadione, D-(+)-glucose were purchased from Wako Pure Chemicals Industries, Ltd. Ferrocene methanol ($FcCH_2OH$) was purchased from Sigma Aldrich. All solutions were prepared using distilled and deionized water from Direct-Q (Millipore).

2.2 Yeast Strain and Growth Conditions

Saccharomyces cerevisiae strain Y190 was donated by Dr. Fujio Shiraishi from the National Institute for Environmental Studies. The cells were cultured for 24 h at 30 °C with shaking at 100 rpm in modified SD medium (without tryptophan and leucine) [17]. The culture was collected as a pellet by centrifugation (6000 rpm for 5 min), washed twice with Z buffer (60.0 mM $Na_2HPO_4{\cdot}12H_2O$; 39.7 mM $NaH_2PO_4{\cdot}2H_2O$; 10.0 mM KCl; 10.0 mM $MgSO_4{\cdot}7H_2O$; pH 7.0), and then resuspended in Z buffer.

2.3 Fabrication of Pt Micro- and Nanoelectrodes

The fabrication of the Pt microelectrode was described previously [29]. A Pt nanoelectrode was fabricated by simultaneously pulling a quartz capillary and a Pt wire inserted into the capillary under vacuum using a CO_2 laser puller P-2000 (Sutter) [30–32]. First, an annealed Pt wire (25.0 μm diameter) was inserted into the middle of 100 mm long quartz capillary (1.0 mm outer diameter and 0.3 mm inner diameter). Then, the Pt wire was sealed into the quartz capillary by irradiating CO_2 laser to the middle of the capillary under the following parameters: heat=960, filament=4, velocity=100, delay=120 and pull=0. The heating process was carried out for 30 s followed by a cooling time of 30 s. For tight sealing of the Pt wire into the capillary, the heating process was performed under reduced pressure by connecting each end of the quartz capillary to a vacuum line. The heating/cooling process was repeated 5 times to ensure a proper sealing. Later, the capillary was pulled under the following parameters to form two sets of Pt nanoelectrodes: heat=885, filament=2, velocity=50, delay=100, and pull=100. A copper lead wire was inserted into the capillary to make an electrical connection with the Pt wire using a silver paste. Finally, the tip of the nanoelectrode was carefully polished using a diamond grinder (EG-6, Narishige) to expose the disk-shaped active surface of the Pt wire.

2.4 SECM Imaging of NOEs Activity in Bulk Yeast Cells

Yeast cells (4×10^4) were entrapped in a cylindrical-shaped poly(dimethylsiloxane) (PDMS) microwell (diameter, 450 μm; depth, 50 μm). The fabrication method of the PDMS microwell array has been described previously [17]. The suspension of yeast cells was dispersed on the PDMS microwell array and stabilized for 10 min until the cells were dropped into the wells. The excess yeast cells were removed by washing the surface of the PDMS microwell array with Z buffer two times. Finally, the measurement solution was poured on the PDMS microwell array for SECM measurements. The components of the measurement solution were as follows: 20 mM potassium hexacyanoferrate(III), 0.10 mM menadione, and 20 mM D-(+)-glucose in Z buffer.

Imaging experiments were carried out using a SECM system including an inverted microscope (TE300, Nikon), a current amplifier (Model 427, Keithley), a stepping motor-driven XY stage (Model D70, Suruga Seiki), and a piezoelectric motor-driven Z stage (E-501, Physik Instrumente). For positioning, the Pt probe microelectrode (Pt radius, 7.4 μm) was brought into contact with the substrate surface. From there the probe was vertically retracted 20.0 μm off the surface using the piezoelectric motor with a precision of 0.1 μm. The potential of the probe electrode was held at +0.60 V vs. Ag/AgCl to provide a steady-state oxidation current for reduced form of mediator. The electrode was vertically scanned from the

original set position to 1.0 mm away from the PDMS surface at a scan rate of 9.5 $\mu m\,s^{-1}$ to detect the ferrocyanide concentration profile formed around the microwell containing yeast cells.

2.5 SECM Imaging of NOEs Activity in Single or Several Yeast Cells

Single or groups of yeast cells were electrostatically immobilized on an aminosilanized glass (Matsunami Glass Ind. Ltd.). The suspension of yeast cells was dispersed on the glass substrate and stabilized for 10 min to allow attachment on the surface of the glass. Excess yeast cells were removed by washing the surface of the slide glass with Z buffer twice, followed by pouring the measurement solution on the slide glass. The measurement solution was Z buffer containing 20 mM potassium hexacyanoferrate(III), 0.10 mM menadione, and 20 mM D-(+)-glucose. The Pt probe micro- or nanoelectrode was positioned 7.0 μm above the substrate surface with a precision of 0.1 μm in vertical direction. The probe electrode was laterally scanned over yeast cells at a scan rate of 1.0 $\mu m\,s^{-1}$ to detect the concentration profile of ferrocyanide around the cells. The potential of the probe electrode was held at +0.60 V vs. Ag/AgCl to detect the oxidation current for ferrocyanide. The time required for SECM imaging at an area of $30\times30\ \mu m^2$ (spatial resolution, 1.0 μm) was approximately 30 min.

2.6 Quantitative Analysis of Mass Transfer Rate of Redox Mediator from Single Yeast Cell Using GC Mode SECM Imaging

Quantification of the mass transfer rate of the redox mediator from single yeast cell was carried out using GC mode SECM imaging as described previously [33]. When a spherically shaped cell is positioned on a flat substrate in a measurement solution, the mass transfer rate of the hemispherically diffusing redox mediator from the yeast cell (F_{yeast} in $mol\,s^{-1}$) in a steady-state rate can be estimated by multiplying the flux at a certain point ($f_{r=rx}$ in $mol\,cm^{-2}\,s^{-1}$, r refers to the distance from the cell surface) with the semi-spherical section area ($S_{r=rx}$ in cm^2)

$$F_{yeast} = f_{r=rx} \times S_{r=rx} \quad (1)$$

The $S_{r=rx}$ value is expressed as follows:

$$S_{r=rx} = 2\pi\, r_x^2 \quad (2)$$

At $r=r_x$, the flux is expressed as

$$f_{r=rx} = D\ (\Delta C_{r=rx}/\Delta r) \quad (3)$$

Where D is the diffusion coefficient of a redox mediator (for ferrocyanide, $D_{ferro}=6.5\times10^{-6}\ cm^2\,s^{-1}$); $\Delta C_{r=rx}/\Delta r$ is the concentration gradient of the redox mediator, and $\Delta C_{r=rx}$ and Δr are expressed as

$$\Delta C_{r=rx} = |\ C_{r=rx} - C_{r=rx+\Delta r}\ | \quad (4)$$

$$\Delta r = |r_{r=rx} - r_{r=rx+\Delta r}\ | \quad (5)$$

The concentration gradient of a redox mediator at $r=r_x$ is calculated from the profiles of the redox current. The redox current observed with the SECM system is expressed by

$$I_{r=rx} = 4nFDC_{r=rx}\,a \quad (6)$$

Where n is the number of electrons per molecule reduced; F is the Faraday constant ($96500\ C\,mol^{-1}$); $C_{r=rx}$ is the local concentration of the redox mediator at $r=r_x$ ($mol\,cm^{-3}$); and a is the electrode radius (cm).

For SECM imaging using a dual mediator system, it was assumed that menadione is localized within the yeast cell and ferricyanide is outside of the cell. When the ferricyanide concentration is in large excess over the menadione concentration, menadione should not be detected directly with a SECM probe electrode because all the menadione is reoxidized by ferricyanide at the cell surface. If we assume that the concentration of menadione and ferricyanide is in large excess over the Michaelis constant value of NOEs and that the SECM probe detects the diffusion-limited current, the rate-limiting step for determining current response is the cellular reaction step including NOEs reaction rate and the permeation rate of mediator through the cell membrane [34].

3 Results and Discussion

Figure 2A shows the scanning electron micrograph (SEM) of the tip of the Pt nanoelectrode. The nanometer-sized Pt disk was clearly identified at the center of the insulating quartz sheath. At higher magnification, the radius of the Pt disk was determined to be approximately 300 nm (Figure 2B). Figure 2C shows a cyclic voltammogram (CV) of 0.50 mM $FcCH_2OH$ detected with the Pt nanoelectrode shown in Figure 2A. At the potential scan rate of 20 mV/s, CV showed a s-shaped curve with the steady-state current at +0.50 V vs. Ag/AgCl. Assuming the geometry of the nanoelectrode to be disk shaped, the steady-state current for a nanoelectrode in an insulating sheath is given by Equation 6 with the diffusion coefficient of $FcCH_2OH$ as $7.8\times10^{-6}\ cm^2\,s^{-1}$ [32] and the bulk concentration of $FcCH_2OH$ as $5.0\times10^{-7}\ mol\,cm^{-3}$. Using Equation 6, the radius of the nanoelectrode was calculated as 380 nm, which was almost the same size as the identified size from SEM observation.

Figure 3A shows the responses of 4×10^4 yeast cells entrapped in a PDMS microwell in 20 mM D-(+)-glucose solution containing (a) 20 mM ferricyanide, (b) 0.10 mM menadione, and (c) 20 mM ferricyanide and 0.10 mM menadione. The ordinate in Figure 3A represents the current change when the electrode set at +0.60 V vs. Ag/AgCl was vertically scanned from the original set position

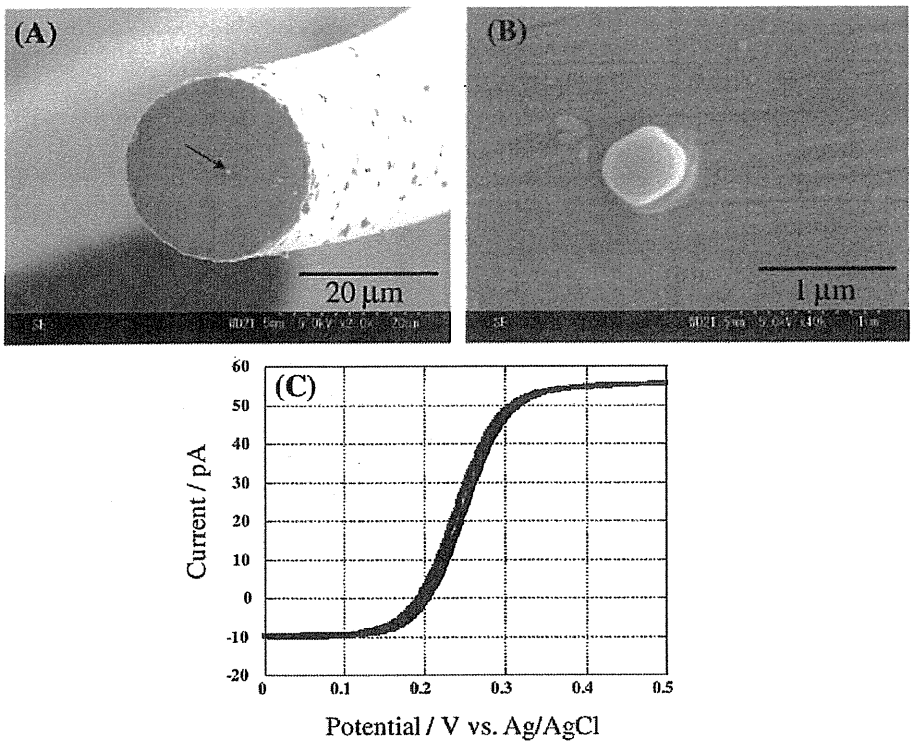

Fig. 2. A) Scanning electron micrograph of the tip of a Pt nanoelectrode. B) Pt disk of the same nanoelectrode as (A) at a higher magnification. C) Cyclic voltammogram of 0.50 mM $FcCH_2OH$ using the Pt nanoelectrode shown in (A). Scan rate: 20 $mV s^{-1}$.

(20.0 μm above the PDMS well surface) to 1.0 mm above from the well surface. When the solution contained only ferricyanide (Figure 3Aa), the current change was only several pA and almost no current variation was observed on scanning the electrode. This suggests almost no interaction of ferricyanide with the intracellular redox processes due to low permeability of hydrophilic ferricyanide through the yeast cell membrane. In the case of lipophilic menadione (Figure 3Ab), on the other hand, the current change became larger (48 pA). Menadione functions as a permeable redox mediator to interact with NOEs to form menadiol which diffuses into the solution to reduce ferricyanide to give oxidation current at the electrode probe (see Figure 1) [9]. In a dual mediator system (Figure 3Ac), the current change was 2.3 times higher than that with menadione alone in the solution. This tendency was in accordance with previous reports [5,6,9], which suggested that the enhancement of current change in the dual mediator system would attribute to the redox cycling reaction of menadione between ferricyanide and intracellular NOEs depicted in Figure 1 and the help of ferricyanide to overcome the slow heterogeneous redox kinetics of menadione on Pt electrodes [9].

For quantitative analysis of the mass transfer rate of the ferrocyanide from single yeast cell, we examined the concentration of the mediators in large excess over the Michaelis constant value of NOEs. Figure 3B shows the relationship between the mediator concentration and the current change in a dual mediator system. The current change was detected as described in Figure 3A. Each point in Figure 3B has relatively large error bar, because the differences in individual cellular activity caused variation of averaged activity of the cell population depending on the microenvironmental conditions. In Figure 3Ba, the current change tended to be saturated when the concentration of ferricyanide was higher than 1.0 mM in the presence of 0.10 mM menadione. When it was assumed that all of the 1.0 mM ferricyanide was reduced to ferrocyanide by menadiol and the ferrocyanide was oxidized at the 7.4 μm-radius tip in the bulk solution, the calculated oxidation current for ferrocyanide using the Equation 6 is 1.86 nA. This value is much larger than the current change for ferrocyanide generated from the cells in Figure 3Ac (48 pA) even when using 20 mM ferricyanide. These results suggested that more than 1.0 mM of ferricyanide concentration is in large excess over the Michaelis constant value of NOEs. In Figure 3Bb, the current changes increased with increase the menadione concentration and retarded at the concentration higher than 0.20 mM in the presence of 20 mM ferricyanide. Then, the current change gradually decreased when the cells were exposed to the solution containing more than 0.20 mM menadione. This behavior suggests the cytotoxicity of menadione or rapid exhaustion of NAD(P)H [9]. On the basis of these results, the concentrations of menadione and ferricyanide were set to 0.10 mM and 20 mM, respectively, for the dual mediator system.

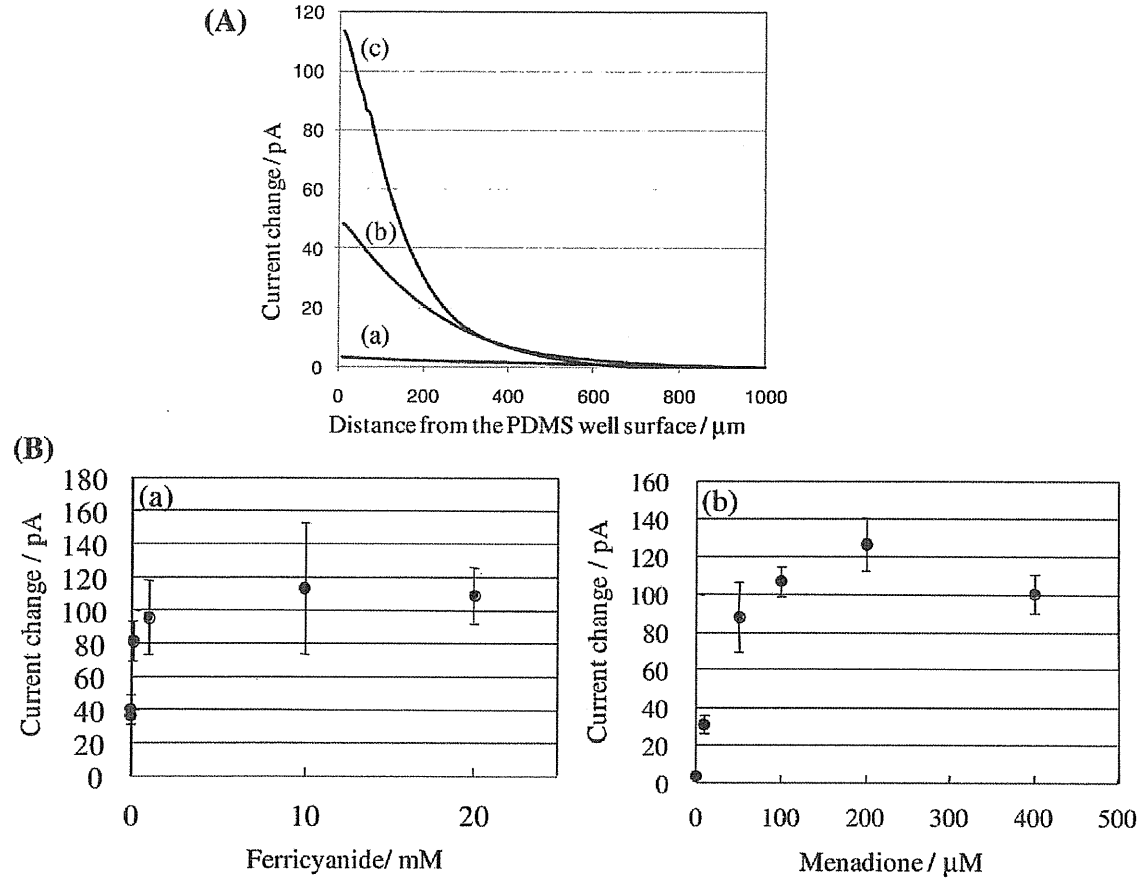

Fig. 3. A) Current changes when a Pt microelectrode probe retracted from 20 μm to 1.0 mm above from the PDMS microwell surface entrapped with 4×10^4 yeast cells in 20 mM D-(+)-glucose solution containing (a) 20 mM ferricyanide, (b) 0.10 mM menadione, and (c) 20 mM ferricyanide and 0.10 mM menadione. B) Current changes vs. concentration plots for (a) ferricyanide and (b) menadione. (a): Concentration of menadione was set at 0.10 mM. (b): Concentration of ferricyanide was set at 20 mM. Each point represents the mean of five measurements ± *SD*. Probe: Pt microelectrode with Pt radius of 7.4 μm. Potential of the probe: +0.60 V vs. Ag/AgCl.

Figure 4 shows the line scan responses for the dual mediator system of 4 aggregated yeast cells when a probe electrode with a Pt radius of (a) 11.9 μm, (b) 1.0 μm, or (c) 199 nm was scanned 7.0 μm above the surface of the glass substrate, together with the optical image of the cells. All the lines show peaks of oxidation current corresponding to the NOEs activity of yeast cells, although the change in the current from the baseline became small with decreasing tip size. The generation rate of ferrocyanide from a single yeast cell, F_{yeast}, was calculated based on Equation 1 and was found to be 3.07×10^{-19} (11.9-μm tip), 1.69×10^{-19} (1.0-μm tip), and 1.73×10^{-19} (199-nm tip) mol s^{-1} cell^{-1}. The generation rates detected using probes with 1.0 μm or 199 nm radii were almost identical and in good agreement with the value previously reported [5]. The oxidation rate for ferrocyanide at the probe electrode, F_{tip}, was calculated based on Equation 6 and found to be 8.05×10^{-20} (1.0-μm tip) and 1.73×10^{-20} (199-nm tip) mol s^{-1} at the peaks in Figure 4B. As F_{tip} at the 199-nm tip was sufficiently smaller than F_{yeast}, the ferrocyanide concentration profile around the cells would not be disturbed by the electrochemical reaction at the tip. However, each single cellular activity could not be resolved from the current response due to crossover of the ferrocyanide diffusion layers around the yeast cells. For the 11.9-μm tip, a large amount of ferrocyanide generated from a yeast cell would be consumed at the probe electrode ($F_{tip}=1.63\times10^{-18}$ mol s^{-1}). Therefore, local concentrations of ferrocyanide could not be precisely measured.

The signal-to-noise ratios in Figure 4B were 23.0 (signal = 668.1 fA, noise = 29.0 fA) for the 11.9-μm tip, 1.7 (signal = 29.0 fA, noise = 17.2 fA) for the 1.0-μm tip, 0.5 (signal = 14.3 fA, noise = 27.1 fA) for the 199-nm tip. Although the noise is in the range of the signal when using nanoelectrode, the increase of oxidation current for ferrocyanide was reproducibly detected around the yeast cells, suggesting the significant current response of the cells was detected using nanoelectrode.

The SECM measurements enabled the visualization of NOEs activity of an isolated single cell. Figure 5 shows the SECM image of a single yeast cell based on oxidation current for ferrocyanide in dual mediator system with the

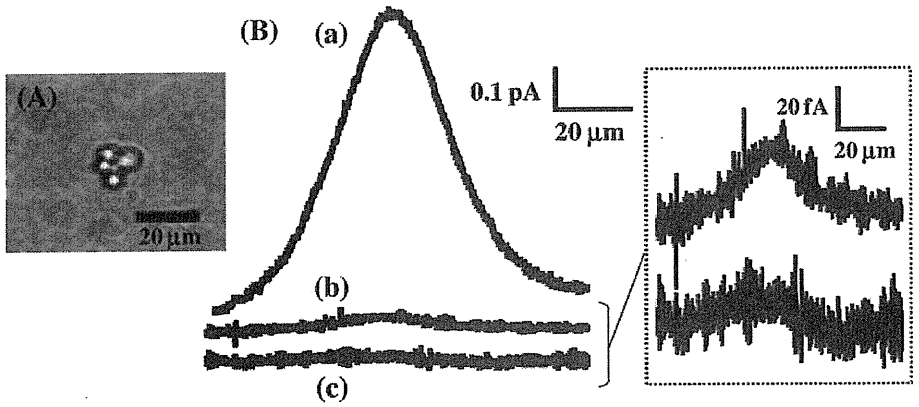

Fig. 4. A) The micrograph of 4 yeast cells. B) Current responses in line-scan images for 4 yeast cells in 20 mM D-(+)-glucose solution containing 20 mM ferricyanide and 0.10 mM menadione. Probe: Pt electrode with a Pt radius of (a) 11.9 μm, (b) 1.0 μm, and (c) 199 nm. Scan rate: 1.0 $\mu m s^{-1}$. Potential of the probe: +0.60 V vs.Ag/AgCl.

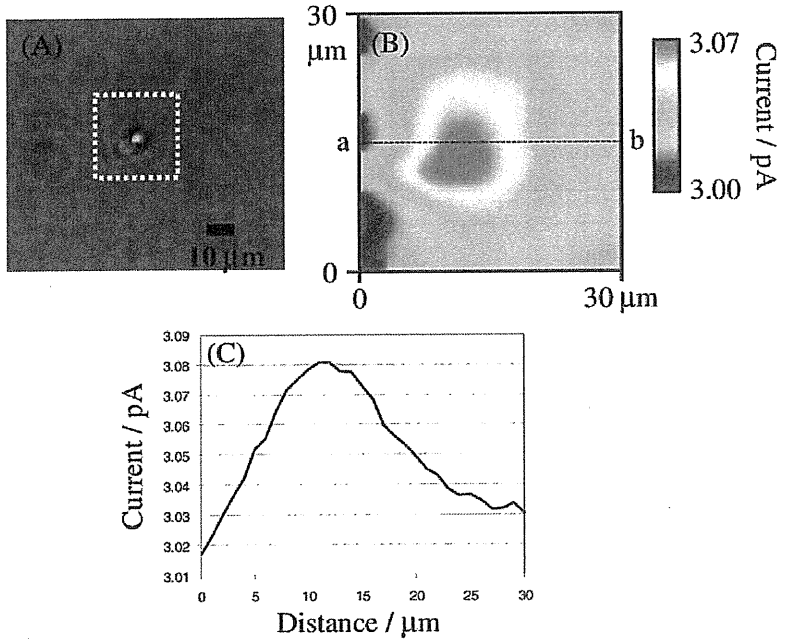

Fig. 5. A) Micrograph of a single yeast cell. B) SECM image of single yeast cell based on oxidation current for ferrocyanide in 20 mM D-(+)-glucose solution containing 20 mM ferricyanide and 0.10 mM menadione. C) Line scan along the cross section a–b in (B). Probe: Pt nanoelectrode with the Pt radius of 450 nm. Potential of the probe: +0.60 V vs. Ag/AgCl. Scan rate: 1.0 $\mu m s^{-1}$.

electrode probe of 450 nm-tip, together with an optical image of the cell. The enhanced current around the cell clearly indicated the NOEs activity of the yeast cell in Figure 5B. Figure 5C shows the line scan along the cross section a-b in Figure 5B. The signal-to-noise ratio calculated from the line scan was 7.7 (signal = 63.7 fA, noise = 8.24 fA), suggesting a significant response of the single yeast cell. Half-width of the current profile for ferrocyanide was found to be 14 μm, which was significantly larger than the size of yeast cell (5.0 μm in diameter). It should be noted again that, regardless of tip diameter, single-cell level resolution in cell aggregates is difficult in the present constant-height GC mode SECM imaging due to spread of the ferrocyanide diffusion layer around the cell.

4 Conclusions

Influence of tip reaction on the GC mode SECM imaging of a single yeast cell was investigated by using various Pt electrode probes with tip sizes in μm–nm scales. The quantitative imaging of NOEs activity in an isolated yeast cells was successfully achieved in the GC mode measurements using the 199 nm-tip without disturbing the mediator concentration profile formed around the cells by the

tip reaction. However, spatial resolution of the SECM image was not improved even when the tip size was downscaled due to spread of the ferrocyanide diffusion layer around the cell. To obtain higher resolution of single cellular images in GC mode, one has to incorporate an accurate cell-benign distance control mechanism at nanometer scale into the SECM system. We think a shear-force or an ion-conductance feedback control is the probable candidate for the distance control. Using these distance control mechanisms, topographic and electrochemical images of locally immobilized cells were captured simultaneously in nanometer-order resolution using standing approach mode SECM [19–22]. In the future, the SECM system with a cell-benign distance control will be applied for characterization of single live yeast cells in a densely-packed population.

Acknowledgements

This work was partly supported by Grants-in-Aid for Scientific Research (18101006, 9750055, 22245011) from *MEXT* (*Ministry of Education, Culture, Sports, Science and Technology*), Japan and by a grant from the *Center for Interdisciplinary Research, Tohoku University.* K. N. acknowledges *G-COE.*

References

[1] M. A. Aon, S. Cortassa, K. M. Lemar, A. J. Hayes, D. Lloyd, *FEBS Lett.* **2007**, *581*, 8.
[2] D. B. Murray, M. Beckmann, H. Kitano, *Proc. Natl. Acad. Sci. USA* **2007**, *104*, 2241.
[3] Z. Palkova, L. Vachova, *FEMS Microbiol. Rev.* **2006**, *30*, 806.
[4] C. T. Parker, V. Sperandlo, *Cell. Microbiol.* **2009**, *11*, 363.
[5] K. H. R. Baronian, A. J. Downard, R. K. Lowen, *Appl. Micribiol. Biotechnol.* **2002**, *60*, 108.
[6] A. Heiskanen, J. Yakovleva, C. Spegel, R. Taboryski, M. Koudelka-Hep, J. Emneus, T. Ruzgas, *Electrochem. Commun.* **2004**, *6*, 219.
[7] A. Heiskanen, C. Spegel, N. Kostesha, S. Lindahl, T. Ruzgas, J. Emneus, *Anal. Biochem.* **2009**, *384*, 11.
[8] J. D. Rabinowitz, J. F. Vacchino, C. Beeson, H. M. McConnel, *J. Am. Chem. Soc.* **1998**, *120*, 2464.
[9] C. F. Spegel, A. R. Heiskanen, N. Kostesha, T. H. Johanson, M. F. G. Grauslund, M. Koudelka-Hep, J. Emnus, T. Ruzgas, *Anal. Chem.* **2007**, *79*, 8919.
[10] J. Zhao, M. Wang, Z. Yang, Z. Wang, H. Wang, Z. Yang, *Anal. Chim. Acta* **2007**, *597*, 67.
[11] C. Amatore, S. Arbault, M. Erard, *Anal. Chem.* **2008**, *80*, 9635.
[12] C. Cai, B. Liu, M. V. Mirkin, H. A. Frank, J. F. Rusling, *Anal. Chem.* **2002**, *74*, 114.
[13] W. Feng, S. A. Rotenberg, M. V. Mirkin, *Anal. Chem.* **2003**, *75*, 4148.
[14] D. T. Pierce, A. J. Bard, *Anal. Chem.* **1993**, *65*, 3598.
[15] H. Shiku, T. Shiraishi, H. Ohya, T. Matsue, H. Abe, H. Hoshi, M. Kobayashi, *Anal. Chem.* **2001**, *73*, 3751.
[16] H. Shiku, T. Shiraishi, S. Aoyagi, Y. Utsumi, M. Matsudaira, H. Abe, H. Hoshi, S. Kasai, H. Ohya, T. Matsue, *Anal. Chim. Acta* **2004**, *522*, 51.
[17] H. Shiku, S. Goto, S. Jung, K. Nagamine, M. Koide, T. Itayama, T. Yasukawa, T. Matsue, *Analyst* **2009**, *134*, 182.
[18] P. Sun, F. O. Laforge, T. P. Abeyweera, S. A. Rotenberg, J. Carpino, M. V. Mirkin, *Proc. Natl. Acad. Sci. USA* **2008**, *105*, 443.
[19] Y. Takahashi, Y. Hirano, T. Yasukawa, H. Shiku, H. Yamada, T. Matsue, *Langmuir* **2006**, *22*, 10299.
[20] Y. Takahashi, T. Miyamoto, H. Shiku, R. Asano, T. Yasukawa, I. Kumagai, T. Matsue, *Anal. Chem.* **2009**, *81*, 2785.
[21] Y. Takahashi, H. Shiku, T. Murata, T. Yasukawa, T. Matsue, *Anal. Chem.* **2009**, *81*, 9674.
[22] Y. Takahashi, A. I. Shevchuk, P. Novak, Y. Murakami, H. Shiku, Y. E. Korchev, T. Matsue, *J. Am. Chem. Soc.* **2010**, *132*, 10118.
[23] T. Yasukawa, Y. Kondo, I. Uchida, T. Matsue, *Chem. Lett.* **1998**, *8*, 767.
[24] T. Yasukawa, I. Uchida, T. Matsue, *Biochim. Biophys. Acta, Biomemb.* **1998**, *1369*, 152.
[25] T. Yasukawa, I. Uchida, T. Matsue, *Biophys. J.* **1999**, *76*, 1129.
[26] L. Zhu, N. Gao, X. Zhan, W. Jin, *Talanta* **2008**, *77*, 804.
[27] R. Zhu, S. M. Macfie, Z. Ding, *Anal. Chem.* **2008**, *24*, 14261.
[28] J. Mauzeroll, A. J. Bard, *Proc. Natl. Acad. Sci. USA* **2004**, *101*, 7862.
[29] T. Matsue, S. Koike, T. Abe, T. Itabashi, I. Uchida, *Biochim. Biophys. Acta* **1992**, *1101*, 69.
[30] B. B. Katemann, W. Schuhmann, *Electroanalysis* **2002**, *14*, 22.
[31] Y. Shao, M. V. Mirlin, G. Fish, S. Kokotov, D. Palanker, A. Lewis, *Anal. Chem.* **1997**, *69*, 1627.
[32] P. Sun, M. V. Mirkin, *Anal. Chem.* **2006**, *78*, 6526.
[33] T. Kaya, D. Numai, K. Nagamine, S. Aoyagi, H. Shiku, T. Matsue, *Analyst* **2004**, *129*, 529.
[34] K. Nagamine, T. Kaya, T. Yasukawa, H. Shiku, T. Matsue, *Sens. Actuators B* **2005**, *108*, 676.

DOI: 10.1002/anie.201102796

Scanning Probe Microscopy

Multifunctional Nanoprobes for Nanoscale Chemical Imaging and Localized Chemical Delivery at Surfaces and Interfaces**

*Yasufumi Takahashi, Andrew I. Shevchuk, Pavel Novak, Yanjun Zhang, Neil Ebejer, Julie V. Macpherson, Patrick R. Unwin, Andrew J. Pollard, Debdulal Roy, Charles A. Clifford, Hitoshi Shiku, Tomokazu Matsue, David Klenerman, and Yuri E. Korchev**

The dynamics of chemical and biological processes at interfaces underpin a wide range of phenomena, from surface adsorption and crystal growth to signal transduction at the cell membrane. Since many interfaces have nanoscale structures which control these phenomena, it is vital to be able to perform measurements of chemical and biochemical fluxes on this length scale. One technique with the potential to measure chemically specific fluxes on the nanoscale is scanning electrochemical microscopy (SECM),[1,2] but a lack of reliable distance (feedback) control (in contrast to other scanning probe microscopes) and difficulties in fabricating small-scale electrodes have largely restricted the technique to the micro-scale.[3] Electrochemical imaging on the nanoscale has been demonstrated only rarely[4] and in rather unusual environments.[5,6] There have been various attempts to introduce distance control into SECM by using, for example, shear force,[7–9] intermittent contact (IC) SECM,[10,11] SECM-AFM,[11–14] and the combination of SECM with scanning ion conductance microscopy (SICM).[15,16] While these techniques have the potential to allow electrochemical imaging on the nanoscale, they have the major disadvantage that they require specialist probes which are often difficult and time-consuming to fabricate and use.

Herein, we introduce an extremely quick (<2 min) and simple process with a high success rate for making double-barrel carbon nanoprobes (DBCNPs) for use in SECM-SICM. The overall probe radius is controllable on the nano- to microscale (see below), and the probes can be used for simultaneous chemical and topographical imaging, nano-positioning, and localized chemical delivery and detection by using SICM[17–20] distance feedback control. We first demonstrate its capability with approach curve measurements and by imaging test samples, and then by demonstrating its application to rat adrenal pheochromocytoma cells (PC12) by the simultaneous high-resolution imaging of the topography and electrochemical activity. Finally, exemplar studies of the localized chemical stimulation and detection of neurotransmitter release from PC12 cells by using DBCNPs is reported, which provides a platform for many future applications in cell biology.

DBCNPs were fabricated with one barrel filled with carbon for use as the SECM nanoelectrode, and the other barrel filled with electrolyte for SICM. The double-barrel pipette was pulled from a "theta" quartz capillary. This type of pipette was previously used for SICM and controlled deposition,[21,22] for the electrochemical imaging of electrode surfaces,[23] and for investigation of charge-transfer processes.[24] For SECM-SICM, one barrel was coated internally with carbon, formed in situ by the pyrolytic decomposition of butane;[25–27] the details of the fabrication method are described in the experimental section (Figure 1a). After carbon deposition, electrical contact was established by inserting a conductive wire through the top end of the pipette barrel to contact the carbon layer. The second barrel was unmodified, filled with electrolyte, and used for SICM distance control and chemical delivery (Figure 1b).

The method allows fabrication of DBCNPs with a radius ranging from 10 nm to 1 μm. Examples of field emission scanning electron microscopy (FESEM) images of different-sized electrodes are presented in Figure 1 and Figure S1 in the Supporting Information. The sizes of the DBCNPs are controlled by the initial capillary pulling process, and show high reproducibility; a typical size distribution of DBCNPs is shown in Figure S2 in the Supporting Information. The Supporting Information also contains exemplar studies of voltammetry at these probes, for a range of apparent sizes and

[*] Dr. Y. Takahashi, Dr. A. I. Shevchuk, Dr. P. Novak, Prof. Y. E. Korchev
Division of Medicine, Imperial College London
London W12 0NN (UK)
E-mail: y.korchev@ic.ac.uk
Prof. Y. Zhang
China National Academy of Nanotechnology & Engineering
Tianjin 300457 (China)
N. Ebejer, Prof. J. V. Macpherson, Prof. P. R. Unwin
Department of Chemistry, University of Warwick
Coventry CV4 7AL (UK)
Dr. A. J. Pollard, Dr. D. Roy, Dr. C. A. Clifford
National Physical Laboratory
Teddington TW11 0LW (UK)
Dr. H. Shiku, Prof. T. Matsue
Graduate School of Environmental Studies, Tohoku University
Aramaki Aoba 6-6-11-605, Sendai 980-8579 (Japan)
and
Advanced Institute of Materials Research, Tohoku University
Katahira, Aoba 2-1-1, Sendai 980-8577 (Japan)
Prof. D. Klenerman
Department of Chemistry, Cambridge University
Cambridge, CB2 1EW (UK)

[**] This work was funded by the EPSRC and the Chemical and Biological Programme of the National Measurement System of the UK Department of Business, Innovation, and Skills. Y.T. acknowledges support from JSPS Postdoctoral Fellowships for Research Abroad. P.R.U. thanks the European Research Council for support.

Supporting information for this article is available on the WWW under http://dx.doi.org/10.1002/anie.201102796.

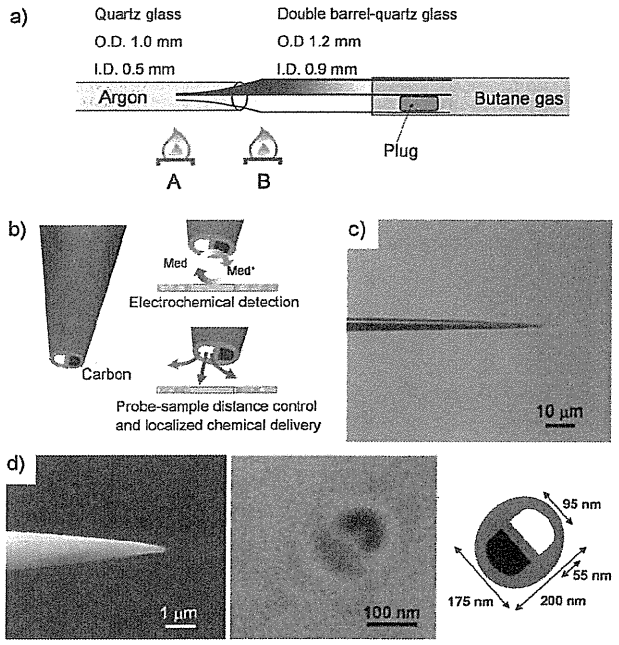

Figure 1. DBCNP fabricated by using the pyrolytic carbon deposition method. a) Schematic illustration of the fabrication method of the DBCNP. b) The principle of combined SECM-SICM measurement with a DBCNP. c) Optical microscopy image of the side view of the DBCNP. d) FESEM images of the side and top of the DBCNP. Note, the carbon deposited inside one of the barrels appears lighter compared to an empty barrel on the FESEM image, but is shown black in the schematic representation (a,b)

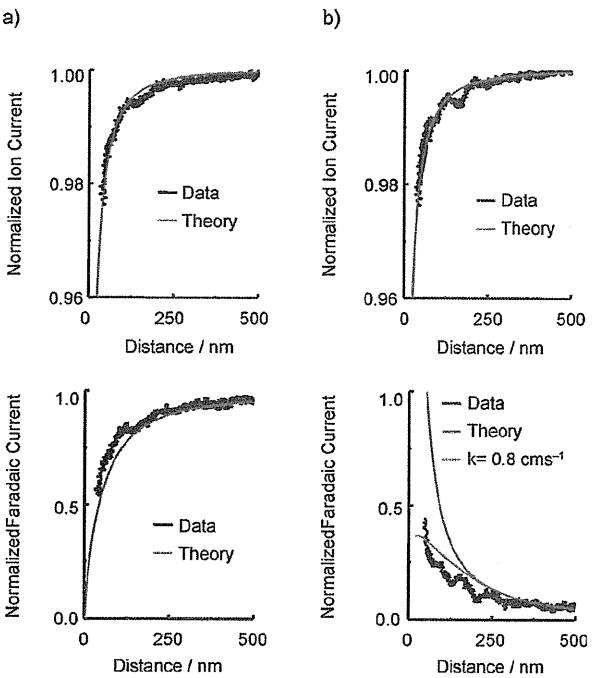

Figure 2. Approach curves of a DBCNP for simultaneous ion current (top) and electrochemical (bottom) measurements on an insulating (a) and conductive (b) substrate in 1.0 mM $FcCH_2OH$ + PBS. The SECM and SICM electrodes were held at 500 and 200 mV versus a reference Ag/AgCl electrode, respectively. The RG value used for the theoretical curves was 1.5.

redox couples, from simple electron transfer to ferrocenylmethanol ($FcCH_2OH$) to fast-scan cyclic voltammetry (FSCV) for the detection of dopamine (Figure S3).

Figure 1c,d show optical and FESEM images of the apex of a typical DBCNP. In this particular case, the effective radii of the SICM aperture and SECM carbon electrode are less than 50 nm and the overall probe radius is only 100 nm. This provides an important advantage for the topographical and electrochemical imaging of cell surfaces, since the probe can access the cell surface and detect areas of slight roughness without unwanted probe-cell contact.[20]

Figure 2a,b show typical experimental approach curves (black lines), for the SECM and SICM channels (recorded simultaneously), with insulating and conducting substrates, respectively. Both channels were fit to established theoretical curves for a simple disk geometry or opening[4,10,28–30] (red lines). This is found to provide a reasonable description of the basic characteristics of the probes, particularly given the idealized (single symmetric channel) of these models compared with the DBCNP geometry, and the fact that the latter will show some non-idealities on the nanoscale. As expected, the ion-current signal decreases for both the insulating and conducting substrates as the distance decreases, thereby highlighting that it can be used for unambiguous distance feedback control.

The SECM approach for the insulating and conducting substrates (Pt interdigitated array electrode (IDA)) showed negative (hindered diffusion) and positive (redox regeneration) feedback responses, respectively.[31] In this case, the electrode radius a was estimated to be 120 nm from the steady-state current in bulk solution and the fact that the negative feedback approach curve fits reasonably well to this value (and RG 1.5 (RG = ratio of the radii of the insulating sheath and the electrode)) indicates that the disks have a good planar geometry, as evident in the FESEM images. Furthermore, it is noteworthy that, by using the ion current feedback distance control, the electrode could approach the substrate as close as 50 nm without making direct contact. While one might expect to see pure positive feedback with an unbiased conductive surface, the experimental data indicate finite regeneration (surface redox) kinetics. Such effects have been seen previously with nanoscale tips at unbiased surfaces[4,10] and can be attributed to the fact that a small tip–substrate separation results in high mass transfer (D/d ca. 2 $cm\,s^{-1}$ at the closest separation d, where D is the diffusion coefficient of the redox species). The characteristic heterogeneous rate constant appears to be of the order of $k = 0.80\ cm\,s^{-1}$; deviations in the fit between experiment and theory can be attributed to non-ideality in the probe geometry.

Importantly, because the SICM channel provides the tip to surface distance, k is the only adjustable parameter when fitting the data. This highlights a key aspect of the SECM-SICM technique: the unambiguous quantitative determination of surface kinetics (and fluxes) because the distance between the tip and surface is known.

To evaluate the resolution of the DBCNP we recorded topographical and electrochemical images of nanopores (pore radii ca. 100 nm) in polyethylene terephthalate (PET) membranes. In our experiment, both sides of the membrane were filled with phosphate-buffered saline (PBS) containing 1.0 mM $FcCH_2OH$. The oxidation current of the $FcCH_2OH$ was recorded simultaneously with the topography by using the DBCNP ($a = 28$ nm); the potentials of the SECM carbon and SICM Ag/AgCl electrodes were 500 and 200 mV, respectively, for this and other test substrates. A constant d value of 30 nm was maintained by the SICM feedback. Figure 3a shows simultaneously recorded topographical and electrochemical images of the PET membrane, with the pore shapes and the electrochemical signals corresponding to the pore positions seen clearly. The decrease in the $FcCH_2OH$ oxidation current indicates that the diffusion of the $FcCH_2OH$ was blocked by the pore (decreased SECM channel current), because the probe moves towards the membrane under SICM feedback control as the probe encounters the pore.

To test the DBCNPs further, SECM-SICM was used to image a Pt IDA (Figure 3b). The d value was maintained at 100 nm by the SICM feedback, so that the SECM current clearly reflects the electrochemical activity of the sample. The oxidation current of the $FcCH_2OH$ was recorded simultaneously with the topography by using a DBCNP ($a = 88$ nm). It is clear that the electrochemical signal increases over the Pt bands (100 nm high in the SICM topography image) because of redox cycling, as for the approach curves in Figure 2c. Importantly, with this design of SECM-SICM probe, the insulation is considerably better (there are no pinholes or recessing of the electrode) and the probe size is smaller than previously reported.[15]

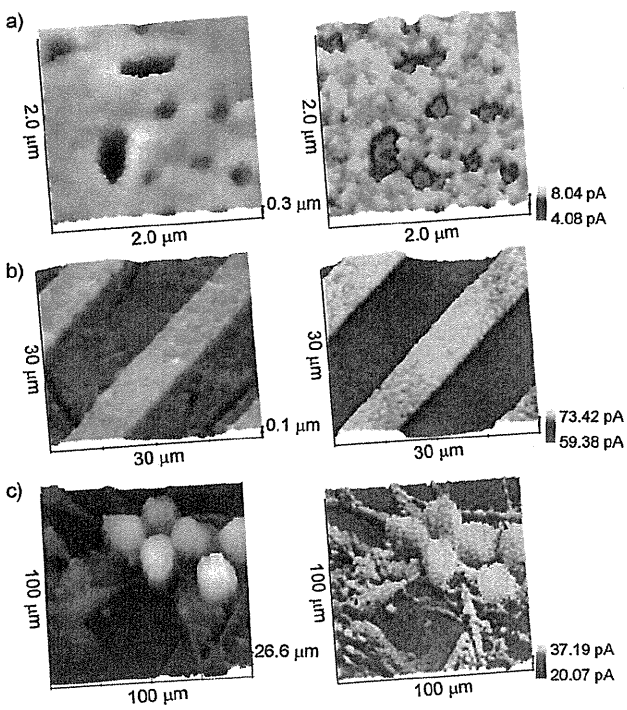

Figure 3. Simultaneous topographical (left) and electrochemical (right) images. a) PET in 1.0 mM $FcCH_2OH$ + PBS. b) Pt interdigitated array in 1.0 mM $FcCH_2OH$ + PBS. c) Living sensory neurons in 0.5 mM $FcCH_2OH$ + HBSS. The SECM and SICM electrodes were held at 500 and 200 mV versus a reference Ag/AgCl electrode, respectively. Electrochemical images were based on an oxidation current of $FcCH_2OH$.

To demonstrate electrochemical and topographical imaging of neurons using DBCNPs ($a = 240$ nm) we visualized the permeation of $FcCH_2OH$, a hydrophobic mediator which can cross the cell membrane, simultaneously with the topography of living sensory neurons. Figure 3c shows the SECM-SICM images of sensory neurons in Hank's buffered salt solution (HBSS) containing 0.5 mM $FcCH_2OH$. The tall cell bodies, exceeding 25 μm in height, and dendritic structures are clearly observed in both the SICM and SECM images, which correlate very well. The SICM images represent the topography, whereas the SECM images measure the flux of $FcCH_2OH$. When the probe is over the bare petri dish, a current of 23 pA is typically recorded, which is the value expected for hindered diffusion. In contrast, when the probe is over the cells, an enhanced current is observed, which approaches the value of 38 pA when the probe is in bulk solution. This finding indicates that the cellular membrane is permeable to $FcCH_2OH$ and that the permeability can be visualized, largely free from topographical effects, because of the independent distance control from SICM. Furthermore, the electrochemical response shows no deterioration in this biological medium. Thus, the DBCNP can be used for localized electrochemical measurements and simultaneous imaging of the surface topography of complex live biological samples.

To further validate the capabilities of SECM-SICM for imaging the topography of living cells we compared the topography of differentiated PC12 cells by using both a DBCNP and a single SICM nanopipette (Figure 4a,b respectively). The topography of neurons[7,32] and release of neurotransmitters have been previously investigated by using shear force distance control SECM[7] and SICM.[32] However, the resolution of these measurements was not sufficient to probe the dendritic structure of the neuron in any detail. In this present study, the radii of the SICM aperture of the DBCNP and the SICM nanopipette were both 50 nm. The quality of the topographic images were comparable: similar dendritic structures, less than 200 nm diameter, were observed on both images (Figure 4a,b, white arrows).

To enhance the sensitivity of the electrochemical detection by the DBCNPs to enable the release of neurotransmitters to be detected it is important to increase the carbon surface area, but not the SICM barrel aperture for distance feedback control. We thus fabricated cylindrically shaped DBCNPs by depositing additional carbon on the outside of the pipette. The method for depositing carbon on the outer surface of the micropipette tip was as described previously,[27] such that the steady-state current measured in 1 mM $FcCH_2OH$ and PBS was 1.85 nA. We then measured the release of neurotransmitter from undifferentiated PC12 cells with this type of probe (Figure 5a). The FESEM image was taken at a tilted angle to show the deposited carbon on the outside of the capillary. A key advantage of the DBCNP is

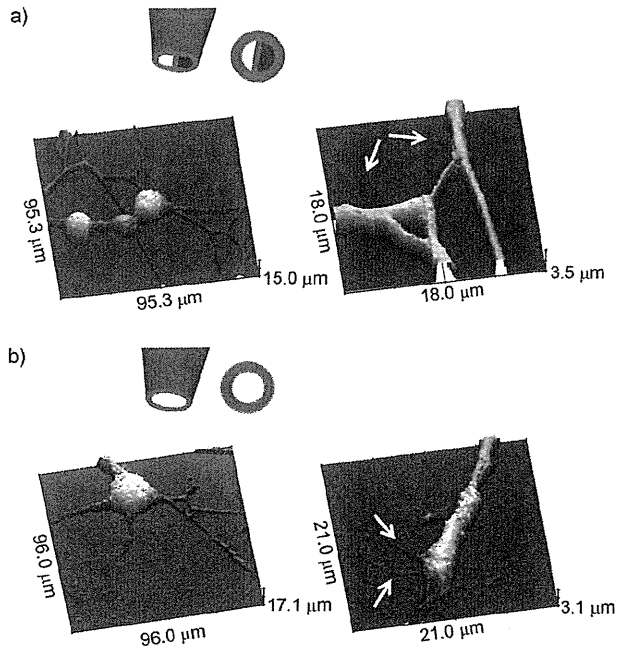

Figure 4. Nanoscale topography images of differentiated PC12 cells using a) the DBCNP and b) a single SICM nanopipette. The arrows showed the dendritic structures.

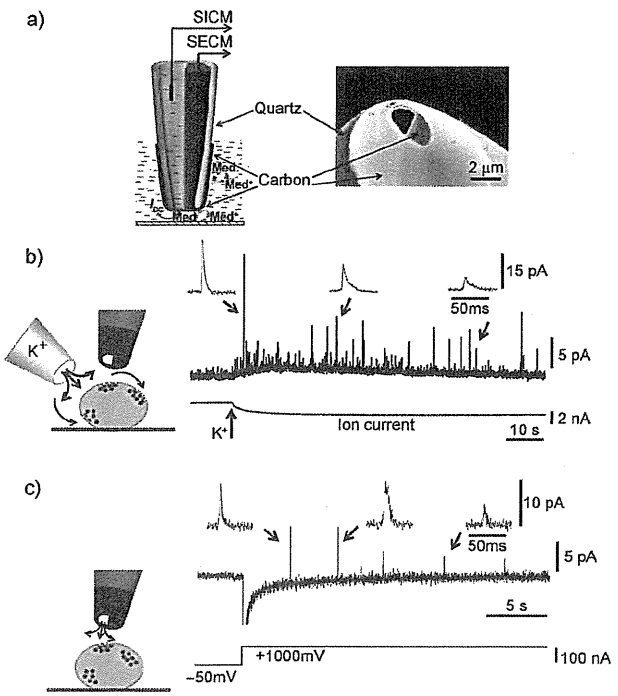

Figure 5. Detection of the release of the neurotransmitter by using the cylindrically shaped DBCNP. a) SEM image of a cylindrically shaped DBCNP. A series of current spikes corresponding to neurotransmitter release detected after b) whole cell stimulation with 105 mM K^+ using another micropipette and c) voltage-driven delivery of K^+ ions using a DBCNP. The carbon electrode was held at 650 mV versus a reference Ag/AgCl electrode.

that it can be positioned with very high precision by using the SICM control: in the present studies it was positioned 500 nm above a PC12 cell.

To stimulate neurotransmitter release we depolarized a PC12 cell by stimulation of the whole cell with 105 mM K^+ by using another micropipette ($a = 3$ µm). Figure 5b shows a series of current spikes corresponding to release of the neurotransmitter which was detected by the probe. The insets of Figure 5b show expanded views of the releasing signal, where the amplitudes and the widths of the spike are clearly visible. It was shown previously that the amplitude and shape of the signal was dependent on the separation between the electrode and release site.[33] It is also possible to observe the increase in local K^+ concentration at the DBCNP by the increase in the negative ion current (Figure 5b, bottom trace).

One of the great advantages of using DBCNPs is that the barrel filled with electrolyte can be used to apply different reagents for local stimulation of the cell: the voltage-driven local chemical change produced by the nanopipette is effective for controlling the function of the biological sample.[34] Therefore, in the next series of experiments we performed voltage-driven application of K^+ ions by using the DBCNP itself to achieve both the local depolarization of the cell membrane and simultaneous detection of the neurotransmitter. With the SICM barrel filled with 3 M KCl, the applied voltage of the SICM electrode was changed from −50 mV to 1000 mV. This ejected potassium ions from the SICM barrel pipette towards the cell surface, thereby inducing local triggering of neurotransmitter release. Figure 5c shows a series of current spikes that were detected after local stimulation with the voltage-driven application of K^+ ions.

With local stimulation we always detected either a low frequency of current spikes compared with whole cell stimulation or no spikes at all. This finding suggests that the DBCNP can be used to induce and detect localized release of the neurotransmitter over the cell surface, thus opening up possibilities to perform the mapping of neurotransmitter release sites.

We have developed a simple, affordable, and quick method of fabricating a DBCNP for functional nanoscale (electro)chemical imaging by using SICM distance feedback control. The fabrication method yields probes with controllable radii in the range of 10 nm to 1 µm with excellent temporal and spatial resolution. Among the many possibilities in the physical and life sciences, this novel probe allows the mapping of sites of neurotransmitter release together with the associated changes in the cell topography that occur during exocytosis, and in the future this technique could be extended to perform intracellular measurements.

Experimental Section

For fabrication of the DBCNP, a quartz theta glass capillary (O.D. 1.2 mm, I.D. 0.9 mm; Sutter Instrument, USA) was pulled using a CO_2 laser puller (model P-2000, Sutter Instrument, San Rafael, CA, USA). Figure 1a shows a schematic illustration of the fabrication system. Butane was passed through the quartz capillary by using a Tygon tube (O.D. 2.4 mm, I.D. 0.8 mm). First, both of the ends of the barrels were blocked with reusable putty-like pressure-sensitive adhesive. Next, one of the barrels was opened and pressurized with butane gas to

deposit carbon inside this barrel only. The other barrel remained blocked and, therefore, no carbon was deposited so that it could be used for SICM. The taper of the pipette was inserted into another quartz capillary (O.D. 1.0 mm, I.D. 0.7 mm; Sutter Instrument, USA), which was filled with argon gas to prevent oxidation of the carbon layer and bending of the capillary by high temperature. This approach also protected the pipette aperture from closing through softening of the quartz pipette walls. To form a pyrolytic carbon layer inside the capillary, the pipette taper was then heated with a Bunsen burner for times ranging from 0.5 s for a 100 nm radius electrode through to 3 s for a 1 μm radius electrode. The deposited layer of carbon inside the pipette is clearly observed in the SEM image of a cross-section of a DBCNP shown in Figure S1c.

To detect release of the neurotransmitter from a PC12 cell, an increase in the carbon surface area was required for enhanced sensitivity of the electrochemical measurement. We, therefore, fabricated cylindrically shaped DBCNPs by depositing carbon on the outside of the top of the tip. Details of the deposition have been described in a previous report.[27] The argon flow (1.2 $L min^{-1}$) is important to control the outside area of carbon deposition. Additionally, the activation of the carbon electrode is also an important process for the detection of neurotransmitters.[35] The DBCNPs were activated by applying −1.0 V versus a reference Ag/AgCl electrode for 1 min.

The DBCNP was difficult to fill with the electrolyte solution because of air plugs that formed close to the pipette taper. To force these air bubbles out of the electrolyte we used a cigarette gas lighter to quickly heat the solution inside the pipette. The heat supplied by the gas lighter was not great enough to soften the quartz walls of the pipette, but resulted in rapid expansion of the air bubble and its movement towards the wider part of the pipette, thereby unblocking the pipette tip. This allowed reliable filling of the pipette with electrolyte.

The SECM-SICM instrument used was similar to one previously described[15] and was operated in a hopping mode.[20] Details of the SECM-SICM instrument, chemicals and materials, and preparation of the cell culture are described in the supporting information.

Received: April 21, 2011
Revised: July 14, 2010
Published online: ■■ ■■, ■■■■

Keywords: biosensors · living cell imaging · nanoelectrodes · scanning probe microscopy · surface analysis

[1] A. Schulte, W. Schuhmann, *Angew. Chem.* **2007**, *119*, 8914; *Angew. Chem. Int. Ed.* **2007**, *46*, 8760.
[2] G. Wittstock, M. Burchardt, S. E. Pust, Y. Shen, C. Zhao, *Angew. Chem.* **2007**, *119*, 1604; *Angew. Chem. Int. Ed.* **2007**, *46*, 1584.
[3] S. Amemiya, A. J. Bard, F. R. F. Fan, M. V. Mirkin, P. R. Unwin, *Annu. Rev. Analyt. Chem.* **2008**, *1*, 95.
[4] F. O. Laforge, J. Velmurugan, Y. X. Wang, M. V. Mirkin, *Anal. Chem.* **2009**, *81*, 3143.
[5] F. R. F. Fan, A. J. Bard, *Proc. Natl. Acad. Sci. USA* **1999**, *96*, 14222.
[6] J. V. Macpherson, P. R. Unwin, *Anal. Chem.* **2000**, *72*, 276.
[7] A. Hengstenberg, A. Blochl, I. D. Dietzel, W. Schuhmann, *Angew. Chem.* **2001**, *113*, 942; *Angew. Chem. Int. Ed.* **2001**, *40*, 905.
[8] Y. Takahashi, Y. Hirano, T. Yasukawa, H. Shiku, H. Yamada, T. Matsue, *Langmuir* **2006**, *22*, 10299.
[9] Y. Takahashi, T. Miyamoto, H. Shiku, R. Asano, T. Yasukawa, I. Kumagai, T. Matsue, *Anal. Chem.* **2009**, *81*, 2785.
[10] K. McKelvey, M. A. Edwards, P. R. Unwin, *Anal. Chem.* **2010**, *82*, 6334.
[11] A. Kueng, C. Kranz, A. Lugstein, E. Bertagnolli, B. Mizaikoff, *Angew. Chem.* **2003**, *115*, 3358; *Angew. Chem. Int. Ed.* **2003**, *42*, 3238.
[12] D. P. Burt, N. R. Wilson, J. M. R. Weaver, P. S. Dobson, J. V. Macpherson, *Nano Lett.* **2005**, *5*, 639.
[13] C. E. Gardner, P. R. Unwin, J. V. Macpherson, *Electrochem. Commun.* **2005**, *7*, 612.
[14] A. Ueda, O. Niwa, K. Maruyama, Y. Shindo, K. Oka, K. Suzuki, *Angew. Chem.* **2007**, *119*, 8386; *Angew. Chem. Int. Ed.* **2007**, *46*, 8238.
[15] Y. Takahashi, A. I. Shevchuk, P. Novak, Y. Murakami, H. Shiku, Y. E. Korchev, T. Matsue, *J. Am. Chem. Soc.* **2010**, *132*, 10118.
[16] D. J. Comstock, J. W. Elam, M. J. Pellin, M. C. Hersam, *Anal. Chem.* **2010**, *82*, 1270.
[17] P. K. Hansma, B. Drake, O. Marti, S. A. C. Gould, C. B. Prater, *Science* **1989**, *243*, 641.
[18] Y. E. Korchev, C. L. Bashford, M. Milovanovic, I. Vodyanoy, M. J. Lab, *Biophys. J.* **1997**, *73*, 653.
[19] A. I. Shevchuik, G. I. Frolenkov, D. Sanchez, P. S. James, N. Freedman, M. J. Lab, R. Jones, D. Klenerman, Y. E. Korchev, *Angew. Chem.* **2006**, *118*, 2270; *Angew. Chem. Int. Ed.* **2006**, *45*, 2212.
[20] P. Novak, C. Li, A. I. Shevchuk, R. Stepanyan, M. Caldwell, S. Hughes, T. G. Smart, J. Gorelik, V. P. Ostanin, M. J. Lab, G. W. Moss, G. I. Frolenkov, D. Klenerman, Y. E. Korchev, *Nat. Methods* **2009**, *6*, 279.
[21] K. T. Rodolfa, A. Bruckbauer, D. J. Zhou, Y. E. Korchev, D. Klenerman, *Angew. Chem.* **2005**, *117*, 7014; *Angew. Chem. Int. Ed.* **2005**, *44*, 6854.
[22] K. T. Rodolfa, A. Bruckbauer, D. J. Zhou, A. I. Schevchuk, Y. E. Korchev, D. Klenerman, *Nano Lett.* **2006**, *6*, 252.
[23] N. Ebejer, M. Schnippering, A. W. Colburn, M. A. Edwards, P. R. Unwin, *Anal. Chem.* **2010**, *82*, 9141.
[24] H. Hu, S. Xie, X. Meng, P. Jing, M. Zhang, L. Shen, Z. Zhu, M. Li, Q. Zhuang, Y. Shao, *Anal. Chem.* **2006**, *78*, 7034.
[25] Y. T. Kim, D. M. Scarnulis, A. G. Ewing, *Anal. Chem.* **1986**, *58*, 1782.
[26] D. K. Y. Wong, L. Y. F. Xu, *Anal. Chem.* **1995**, *67*, 4086.
[27] M. McNally, D. K. Y. Wong, *Anal. Chem.* **2001**, *73*, 4793.
[28] J. L. Amphlett, G. Denuault, *J. Phys. Chem. B* **1998**, *102*, 9946.
[29] M. A. Edwards, C. G. Williams, A. L. Whitworth, P. R. Unwin, *Anal. Chem.* **2009**, *81*, 4482.
[30] Y. H. Shao, M. V. Mirkin, *J. Phys. Chem. B* **1998**, *102*, 9915.
[31] J. Kwak, A. J. Bard, *Anal. Chem.* **1989**, *61*, 1794.
[32] S. A. Mann, G. Hoffmann, A. Hengstenberg, W. Schuhmann, I. D. Dietzel, *J. Neurosci. Methods* **2002**, *116*, 113.
[33] R. M. Wightman, T. J. Schroeder, J. M. Finnegan, E. L. Ciolkowski, K. Pihel, *Biophys. J.* **1995**, *68*, 383.
[34] J. D. Piper, C. Li, C. J. Lo, R. Berry, Y. Korchev, L. M. Ying, D. Klenerman, *J. Am. Chem. Soc.* **2008**, *130*, 10386.
[35] F. G. Gonon, C. M. Fombarlet, M. J. Buda, J. F. Pujol, *Anal. Chem.* **1981**, *53*, 1386.

Communications

Scanning Probe Microscopy

Y. Takahashi, A. I. Shevchuk, P. Novak, Y. Zhang, N. Ebejer, J. V. Macpherson, P. R. Unwin, A. J. Pollard, D. Roy, C. A. Clifford, H. Shiku, T. Matsue, D. Klenerman, Y. E. Korchev* ———— ▮▮▮▮–▮▮▮▮

Multifunctional Nanoprobes for Nanoscale Chemical Imaging and Localized Chemical Delivery at Surfaces and Interfaces

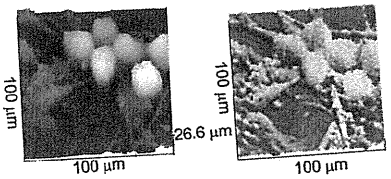

Double take: Double-barrel carbon nanoprobes with integrated distance control for simultaneous nanoscale electrochemical and ion conductance microscopy can be fabricated with a wide range of probe sizes in less than two minutes. The nanoprobes allow simultaneous noncontact topographical (left image) and electrochemical imaging (right) of living neurons, as well as localized K^+ delivery and simultaneous neurotransmitter detection.

Lab on a Chip

Cite this: *Lab Chip*, 2011, **11**, 385

www.rsc.org/loc

COMMUNICATION

Addressable electrode array device with IDA electrodes for high-throughput detection†

Kosuke Ino,*[a] Wataru Saito,[a] Masahiro Koide,[ab] Taizo Umemura,[a] Hitoshi Shiku[a] and Tomokazu Matsue*[a]

Received 23rd September 2010, Accepted 25th November 2010
DOI: 10.1039/c0lc00437e

An electrochemical device is proposed for high-throughput electrochemical detection that consists of 32 row and 32 column electrodes on a single glass substrate. The row and column electrodes are connected to interdigitated array (IDA) electrodes to form 1024 (32 × 32) addressable sensor points in the device. Electrochemical responses from each of the 1024 sensors were successfully acquired on the device within 1 min using redox cycling at individual IDA electrodes, which ensures application of the device to comprehensive, high-throughput electrochemical detection for enzyme-linked immunosorbent assay (ELISA), reporter gene assay for monitoring gene expressions, and DNA analysis.

Recently, the development of array-based biosensors has received a great deal of attention due to the strong demand for rapid, comprehensive, and high-throughput analyses. These techniques take advantage of the two-dimensional layout of recognition elements to allow simultaneous detection and quantification of multiple analytes. Many array-based biosensors are based on fluorescence detection, because fluorescence measurements typically have high sensitivity and a variety of tools for performing the measurements are commercially available. However, fluorescence detection has some disadvantages, such as undesired fluctuations due to quenching or emission from non-target materials, shielding by turbid solution, and the need to label non-fluorescent species, which may cause toxic side effects during analyses. As an alternative method, electrochemical detection has also been incorporated into biosensor devices. The electrochemical signal can be processed by conventional electronics in a very cheap and fast manner. Furthermore, miniaturized electrochemical transducers can easily be integrated in a microsystem by employing conventional microfabrication technologies. In the past decade, various types of amperometric microelectrode arrays have been designed and applied to chemical and biological analyses. These electrochemical array devices have substantial advantages, including rapid response time and qualitative and quantitative detection.[1,2]

Among the various electrochemical arrays, the development of an individually addressable device has been recognized as a key issue to cope with increasing demands for a versatile, reliable and easy-to-use analytical system, especially for comprehensive screening purposes.[3,4] However, it is difficult to collect electrochemical responses at many individual measurement points using a conventional electrochemical device, because sufficient space for the bond pads is not available on the chip border. To solve this problem, we have proposed a novel method to realize individually addressable electrochemical measurement using a device consisting of two sets of microelectrode arrays.[5–8] In the device, two arrays of band microelectrodes are arranged orthogonally face-to-face to fabricate an $n \times n$ array of crossing points (measurement points) with only $2n$ bonding pads for external connection. The crossing points of the column and row electrodes can easily be addressed by setting the potentials at the column and row electrodes to appropriate values. This addressable and multiple detection system has been applied for the detection of enzyme activity[8] and the expression of reporter proteins,[7] and for cell imaging.[5] Although the device is very useful for high-throughput electrochemical detection, careful assembly of the device is required to align two different glass substrates with the row or column electrodes at exact locations upon each measurement, which is time-consuming and results in low reproducibility. Furthermore, there is no open space on the device for handling samples such as cells, because the sensor areas are surrounded by glass substrates with electrodes. In this study, we have developed a new device to solve these problems. The general architecture, outlined in Fig. 1, provides a means for creating a new detection system that enables electrochemical detection based on local redox cycling and 1024 addressable sensor points incorporated into a small area (40 mm^2) for the comprehensive imaging of electrochemical species.

Interdigitated array (IDA) electrodes were incorporated onto glass substrates to arrange a single IDA at each sensor point of the device. IDA electrodes have two interdigitated comb-type arrays, each of which consists of planar and parallel metal fingers.[9] When the potential of each comb-type electrode is appropriately controlled, a species oxidized at an electrode finger can be reduced back at the neighboring fingers, resulting in redox cycling for amplification of the electrochemical signal. In this study, one comb-type electrodes of the IDA connected to a column electrode and the other to a row electrode.

As a first processing step, Ti/Pt was sputtered on glass substrates (50 × 26 mm) to fabricate the row electrodes and IDAs (Fig. 2a and

[a]*Graduate School of Environmental Studies, Tohoku University, Sendai, Japan. E-mail: matsue@bioinfo.che.tohoku.ac.jp; ino.kosuke@bioinfo.che.tohoku.ac.jp*
[b]*Environmental Chemistry Division and Research Center for Environmental Risk, National Institute for Environmental Studies, Tsukuba, Japan*

† Electronic supplementary information (ESI) available: Fig. S1–S4. See DOI: 10.1039/c0lc00437e